Optical properties and electronic structure of the nonmetallic metal FeCrAs

A. Akrap,[1,][*] Y. M. Dai,[1] W. Wu,[2] S. R. Julian,[2,3] and C. C. Homes[1,][†]

[1]*Condensed Matter Physics and Materials Science Department, Brookhaven National Laboratory, Upton, New York 11973, USA*
[2]*Department of Physics, University of Toronto, 60 St. George Street, Toronto, Ontario, Canada M5S 1A7*
[3]*Canadian Institute for Advanced Research, 180 Dundas Street West, Suite 1400, Toronto, Canada M5G 1Z8*

The complex optical properties of a single crystal of hexagonal FeCrAs ($T_N \simeq 125$ K) have been determined above and below T_N over a wide frequency range in the planes (along the b axis) and along the perpendicular (c-axis) direction. At room temperature, the optical conductivity $\sigma_1(\omega)$ has an anisotropic metallic character. The electronic band structure reveals two bands crossing the Fermi level, allowing the optical properties to be described by two free-carrier (Drude) contributions consisting of a strong, broad component and a weak, narrow term that describes the increase in $\sigma_1(\omega)$ below $\simeq 15$ meV. The dc resistivity of FeCrAs is "nonmetallic," meaning that it rises in power-law fashion with decreasing temperature, without any signature of a transport gap. In the analysis of the optical conductivity, the scattering rates for both Drude contributions track the dc resistivity quite well, leading us to conclude that the nonmetallic resistivity of FeCrAs is primarily due to a scattering rate that increases with decreasing temperature, rather than the loss of free carriers. The power law $\sigma_1(\omega) \propto \omega^{-0.6}$ is observed in the near-infrared region and as $T \rightarrow T_N$ spectral weight is transferred from low to high energy ($\gtrsim 0.6$ eV); these effects may be explained by either the two-Drude model or Hund's coupling. We also find that a low-frequency in-plane phonon mode decreases in frequency for $T < T_N$, suggesting the possibility of spin-phonon coupling.

PACS number(s): 78.20.−e, 72.15.−v, 75.50.−y

I. INTRODUCTION

FeCrAs is a rare example of a "nonmetallic metal," a material whose resistivity rises with decreasing temperature but with power-law temperature dependence, as opposed to the exponential rise that signals an insulating gap in the excitation spectrum. Other nonmetallic metals are underdoped cuprates [1,2], some heavy-fermion systems [3], materials on the border of Anderson localization [4], dilute Kondo systems, quasicrystalline metals [5], and the parent compounds of some iron-pnictide superconductors above their magnetic/structural ordering temperatures [6]. In most of these cases, nonmetallic behavior is not understood. FeCrAs is quite an extreme example of nonmetallic behavior [7]: from above 800 K to below 80 mK, the resistivity in the hexagonal (a-b) plane rises monotonically, from ~ 200 $\mu\Omega$ cm at 800 K to ~ 450 $\mu\Omega$ cm at 100 mK, as shown in Fig. 1, where values that are in the metallic range suggest a high carrier density. The c-axis resistivity is similar (Fig. 1), except for a peak just above an antiferromagnetic ordering temperature $T_N \simeq 125$ K that briefly interrupts the rising resistivity.

Moreover, as $T \rightarrow 0$ K, the resistivity does not saturate. Rather, it continues to rise with a sublinear power law. This is in contrast, for example, to dilute Kondo systems in which the resistivity saturates as $\rho(T) = \rho_0 - AT^2$, which is behavior that Nozières explained as indicative of the Fermi-liquid ground state that is expected at temperatures low enough that internal degrees of freedom are locked [8]. Also, the thermodynamic properties of FeCrAs at low temperature *are* Fermi-liquid-like, but quite enhanced, with a large T-linear

specific heat $C(T)/T \sim 30$ mJ/mole K^2 and a correspondingly large Pauli-like magnetic susceptibility $\chi(T)$, leading to a Wilson ratio of $R_W \simeq 4$, as opposed to the expected value of 2 for a Kondo system [7]. This combination of nonmetallic, non-Fermi-liquid transport with Fermi-liquid thermodynamic properties is very unusual.

The hexagonal crystal structure of FeCrAs, shown in the inset of Fig. 1, has a number of triangular motifs that suggest magnetic frustration. The Fe sublattice is a triangular lattice of trimers, while the Cr sites form a distorted Kagome lattice of corner-sharing triangles. Moreover, the antiferromagnetic order is typical of frustrated metallic magnets, being an incommensurate spin-density wave with no detectable ordered moment on the Fe site and the Cr ordered moment varying between 0.6 and 2.2 μ_B throughout the magnetic unit cell, which has an in-plane lattice parameter that is three times larger than the paramagnetic unit cell [9]. In a recent study [10], pressure was used to suppress the magnetic ordering transition, and it was demonstrated that formation of a spin-density-wave gap does not play a decisive role in the anomalous transport properties of this material. It is, however, quite possible that magnetic frustration is important, as recently suggested by Rau *et al.* [11], who put forward a theory that the anomalous behavior of FeCrAs arises from a "hidden spin liquid" on the iron sublattice. In this model, the non-Fermi-liquid, nonmetallic behavior arises from strong charge fluctuations on the Fe sublattice due to proximity to a metal-insulator transition.

An alternative scenario that has been proposed for FeCrAs [12,13] is that it is a "Hund's metal" [14–16], a model that grew out of efforts to explain the electronic properties, including incoherent transport, in superconducting iron pnictides and iron chalcogenides. Dynamical mean-field-theory calculations for these systems suggest that local Hund's rule correlations in the occupancies of the d orbitals, combined with

---

[*]Present address: University of Geneva, CH-1211 Geneva 4, Switzerland.
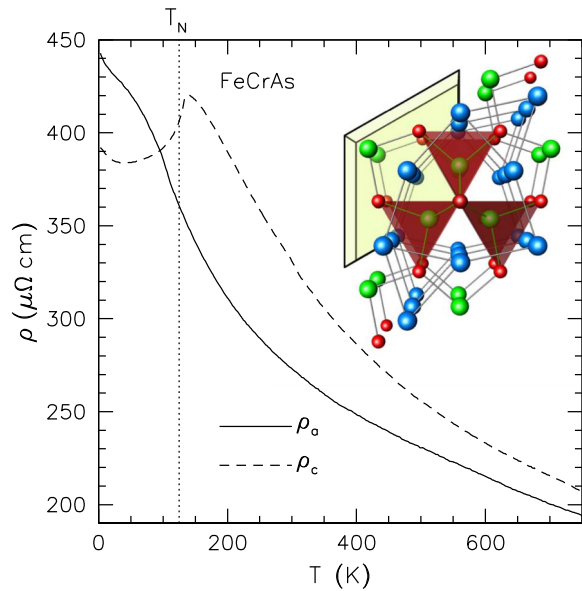
[†]homes@bnl.gov

FIG. 1. (Color online) The resistivity of FeCrAs along the *a* axis (solid line) and *c* axis (dashed line); along the *c* axis, there is an anomaly just above $T_N \simeq 125$ K (dotted line). The inset shows the projection of the extended unit cell of FeCrAs along the crystallographic *c* axis (onto the hexagonal *a-b* plane). The unit cell is indicated by the tinted region. The polyhedra indicate the As (red) coordination around the Fe atoms (green), with the Cr atoms (blue) also forming corner-sharing triangles.

destructive interference between direct and indirect hopping paths, can result in a subset of the *d* orbitals becoming strongly correlated, or even localized. The result is large local moments coupled to more itinerant electrons [14]. As pointed out in Ref. [12], treating these slowly fluctuating large moments in a Kondo limit is equivalent to the underscreened Kondo model, in which the large magnitude of the spin leads to exponential suppression of the Kondo temperature [12,17]. This model predicts a rising resistivity down to very low temperature, and although there should eventually be a crossover to Fermi-liquid behavior, this may be at unobservably low temperatures if the fluctuating moment is large enough. Calculations have mostly focused on iron sites tetrahedrally coordinated by pnictogens (as in FeCrAs) or chalcogens; however, it should be kept in mind that the large magnetic moment in FeCrAs is on the pyramidally coordinated Cr site. This model predicts that the optical masses should be many times larger than the band masses, and that the Wilson ratio should also be large [15,16], as observed in FeCrAs. The prediction for the optical conductivity is that it will show a fractional power-law dependence on frequency, $\sigma_1(\omega) \propto \omega^{-\alpha}$ with $0 < \alpha < 1$, in the near- and mid-infrared regions [18].

The optical conductivity contains a wealth of information about the transport and electrodynamics of a material [19]. For example, the multiband $A\mathrm{Fe_2As_2}$ ("122") materials [20], where $A =$ Ba, Ca, or Sr, are the parent compounds for a number of iron-based superconductors [21]. These materials are poorly metallic and undergo structural and magnetic transitions at $T_s \simeq 130$–200 K, below which their dc conductivity increases substantially [22,23]. Angle-resolved photoemission

spectroscopy (ARPES) reveals that below T_s, the Fermi surface is partially gapped [24] in response to the formation of a spin-density wave, resulting in a decrease in the density of states at the Fermi level. In spite of this Fermi-surface reconstruction, these compounds remain metallic and show decreasing resistivity at low temperature. This behavior is reflected in the optical conductivity; below T_s, there is a transfer of spectral weight (the area under the conductivity curve) from low to high frequency, indicating the opening of a transport gap and consistent with the partial gapping of the Fermi surface observed in ARPES. The decrease in the low-frequency spectral weight also signals the loss of free carriers; however, this loss is compensated by the dramatic decrease in the scattering rate below T_s, with the net result being a resistivity that decreases at low temperature [25,26]. On the other hand, the presence of strong correlations or strong disorder, such as in the quasicrystal $\mathrm{Al_{63.5}Cu_{24.5}Fe_{12}}$, can lead to a dramatically different conductivity spectrum, where the Drude contribution is almost entirely absent [27,28].

In this paper, we present the temperature-dependent polarized infrared spectra for single-crystal FeCrAs. Electronic structure calculations were also performed which show that this material is expected to be metallic, with two energy bands crossing the Fermi level. We have described this multiband conductor using two free-carrier (Drude) contributions; the first is a strong, broad term, while the second is a weak, narrow component that is necessary to describe the low-frequency behavior. The mid-infrared response is described by two bound excitations. An anisotropic response is observed in both the free-carrier response and low-frequency bound excitation. The conductivity in the mid- and near-infrared regions is assumed to arise from bound (interband) excitations which might mask the carrier response in the incoherent regime; however, we note that a $\sigma_1(\omega) \propto \omega^{-0.6}$ is observed in this energy range, which may lend support to the view that this material is a Hund's metal. The coherent Drude components, however, show a scattering rate whose temperature dependence follows the dc resistivity quite closely, demonstrating that the anomalous nonmetallic resistivity of FeCrAs is primarily due to the anomalous temperature dependence of the scattering rate, rather than localization of charge carriers. In addition to the large-scale electronic structure, sharp features in the conductivity are observed at low frequency that are attributed to the normally active infrared lattice modes. One in-plane lattice mode softens below T_N, suggesting the presence of spin-phonon coupling.

II. EXPERIMENT

Crystals were grown from a stoichiometric melt in an alumina crucible within a sealed quartz tube. The material was melted twice, and then annealed at 900 °C for 150 hours. Sample quality in FeCrAs is revealed by the sharpness of the resistive transition near T_N, the value of T_N, and the onset temperature and magnitude of glassy behavior, in the form of a difference between field-cooled and zero-field-cooled magnetic susceptibility. The crystals used in these measurements were from our highest quality batch [7], in which $T_N \sim 125$ K in susceptibility measurements. There is a sharp cusp in the *c*-axis resistivity about 8 K above
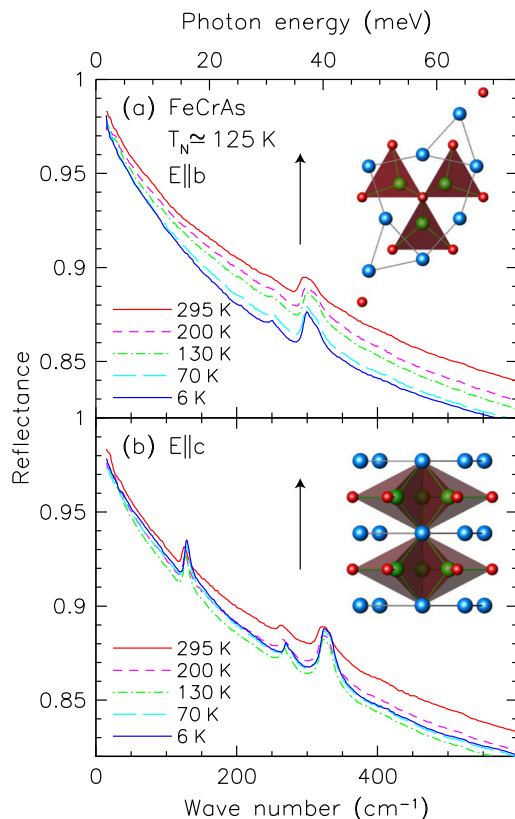
FIG. 2. (Color online) (a) The temperature dependence of the reflectance of a single crystal of FeCrAs for light polarized along the b-axis direction in the infrared region. Inset: The orientation of the electric field along the crystallographic b axis. The Fe, Cr, and As atoms are green, blue, and red, respectively. (b) The reflectance for light polarized along the c axis in the infrared region. Inset: The orientation of the electric field along the crystallographic c axis.

T_N (Fig. 1), and glassy behavior is barely visible and only sets in below 10 K. Further details of crystal growth and characterization can be found in Ref. [29]. The crystal for the infrared measurements was oriented using Laue diffraction, and then cut using spark erosion to expose a flat b-c surface approximately 4.6×1.8 mm, where the longer dimension is along the c axis. The sample was subsequently polished using fine diamond paste, revealing a flat, mirrorlike surface.

The reflectance has been measured at a near-normal angle of incidence over a wide frequency range ($\simeq 2$ meV to 5 eV) for light polarized along the b- and c-axis directions using an overfilling technique and referenced using an *in situ* evaporation method [30]. The low-frequency reflectance is shown in Figs. 2(a) and 2(b) for the b- and c-axis directions, respectively. The orientation of the electric field along the crystallographic direction is shown in the insets. The temperature dependence of the reflectance was measured up to 1 eV, above which the optical properties were assumed to be temperature independent. The polarization dependence of the reflectance was examined up to 3 eV. The low-frequency reflectance for light polarized along the b axis, shown in Fig. 2(a), displays a metallic character, but decreases as the temperature is lowered, in agreement with the increasing resistivity at low temperature. The reflectance along the

c axis, shown in Fig. 2(b), is also metallic and decreasing with temperature; below T_N it increases slightly, again in agreement with transport measurements. The sharp features in the reflectance are attributed to the normally active infrared lattice vibrations (which will be discussed below).

While the reflectance is a useful quantity, it depends on both the real and imaginary parts of the dielectric function, $\tilde{\epsilon}(\omega) = \epsilon_1 + i\epsilon_2$, and can therefore be difficult to interpret. In order to work with more intuitive quantities, the complex dielectric function, and in particular the real part of the complex conductivity, is calculated from a Kramers-Kronig analysis of the reflectance [19]. Because this approach requires that the reflectance be determined over the entire frequency interval, extrapolations must be supplied for $\omega \to 0, \infty$. At low frequency, the material is a poor metal and so the Hagen-Rubens form for the reflectance is employed, $R(\omega) = 1 - a\sqrt{\omega}$, where a is chosen to match the data at the lowest-measured frequency point. While other extrapolations have been considered, e.g., a marginal-Fermi liquid form [34] with $R(\omega) \propto 1 - a\,\omega$, we have determined that the results of the Kramers-Kronig analysis are largely insensitive to the details of the low-frequency extrapolation. Above the highest-measured frequency, the reflectance is assumed to be constant up to 7.5×10^4 cm^{-1}, above which a free-electron gas asymptotic reflectance extrapolation $R(\omega) \propto 1/\omega^4$ is assumed [35].

III. FIRST-PRINCIPLES METHODS AND RESULTS

Electronic structure calculations of FeCrAs were performed within the generalized gradient approximation (GGA) using the full-potential linearized augmented plane-wave (FP-LAPW) method [36] with local-orbital extensions [37] in the WIEN2k implementation [38]. In this instance, it was assumed that the material is paramagnetic and that the spins do not interact. An examination of different Monkhorst-Pack k-point meshes indicated that a $4 \times 4 \times 7$ mesh and $R_{mt}k_{max} = 8.5$ was sufficient for good energy convergence. Initially, the volume of the unit cell was optimized with respect to the total energy. During this process, the c/a ratio was fixed to the experimentally determined value [31–33]. Further geometric optimization was achieved by relaxing the atomic fractional coordinates within the unit cell for the Fe and Cr atoms until the total force was typically less than 1 mRy/a.u. The results of the optimization of the volume and fractional atomic coordinates are summarized in Table I.

TABLE I. The experimental and theoretical lattice constants and atomic fractional coordinates[a] for the optimized structure of FeCrAs in the hexagonal $P\bar{6}2m$ space group. Note that c/a has been fixed to the experimental value.

	Experiment[b]	Theory (GGA)
a(Å)	6.096	5.989
c(Å)	3.651	3.609
Fe ($x0\frac{1}{2}$)	0.2505	0.2522
Cr ($x00$)	0.5925	0.5877

[a]The positions of the As atoms at (000) and ($\frac{1}{3}\frac{2}{3}\frac{1}{2}$) are fixed.
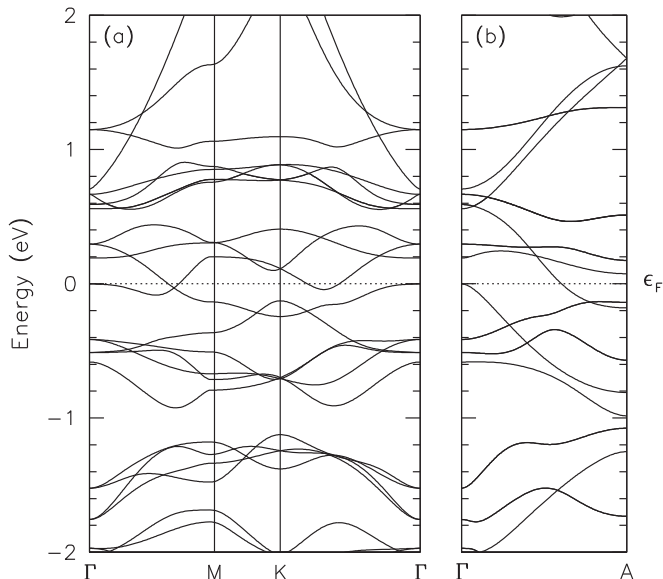[b]References [31–33].

FIG. 3. The electronic band structure of hexagonal FeCrAs close to the Fermi level (ϵ_F) along several high-symmetry paths of a hexagonal unit cell in the (a) k_x, k_y planes and along the (b) k_z direction, respectively. The system is metallic, with two bands crossing ϵ_F.

The electronic band structure along the high-symmetry directions for a hexagonal unit cell near the Fermi level is shown in Fig. 3. Two bands cross the Fermi level (ϵ_F), indicating a metallic system, in agreement with experiment. The orbital character indicates that the bands near ϵ_F are primarily Fe and Cr 3d in nature, while the contribution from the As atoms is negligible. This result is reflected in the density of states (DOS) at the Fermi level, shown in Fig. 4. The total density at ϵ_F is reasonably high, with the main contribution coming from Cr, followed by Fe. The As atoms contribute little or nothing to the DOS at ϵ_F, in agreement with a previous calculation of the density of states [39].

The Fermi surfaces composed of the two bands that cross ϵ_F are shown in Fig. 5. The outer sheet consists of a warped cylinder plus an inner pocket centered on Γ, along the k_z
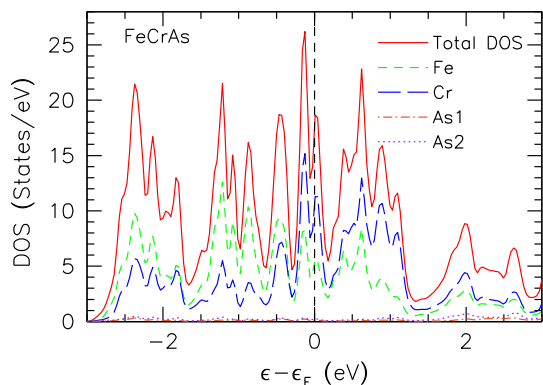

FIG. 4. (Color online) The density of states for FeCrAs close to the Fermi level. The nonzero density of states at ϵ_F indicates a metallic character, with the primary contributions coming from the Cr and Fe atoms, while the As atoms play a small role.
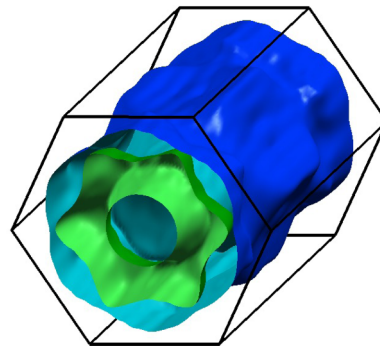

FIG. 5. (Color online) The Fermi surfaces in the Brillouin zone of hexagonal FeCrAs.

projection, while the inner sheet may be described as a distorted torus centered on A.

IV. RESULTS AND DISCUSSION

A. $E \parallel b$

The temperature dependence of the real part of the optical conductivity for light polarized along the b axis is shown over a wide frequency range in Fig. 6(a). The low-frequency conductivity is shown in more detail in Fig. 6(b), where the symbols at the origin denote the values for σ_{dc} determined from transport measurements (Fig. 1). At room temperature, the optical conductivity may be described as a poor metal, with the conductivity displaying a broad maximum at ∼0.5 eV. A standard approach to fitting the optical conductivity in which contributions from both free carriers and a bound excitation are considered is the Drude-Lorentz model for the dielectric function. While the peculiar shape of the optical conductivity below about 15 meV might suggest a renormalization process and therefore the generalized Drude model [40,41], the presence of two bands at the Fermi level precludes its use and instead suggests that contributions from two different types of free carriers should be considered, the so-called two-Drude model [42],

$$\tilde{\epsilon}(\omega) = \epsilon_\infty - \sum_j \frac{\omega_{p,D;j}^2}{\omega^2 + i\omega/\tau_{D,j}} + \sum_k \frac{\Omega_k^2}{\omega_k^2 - \omega^2 - i\omega\gamma_k},$$

(1)

where ϵ_∞ is the real part of the dielectric function at high frequency; $\omega_{p,D;j}^2 = 4\pi n_j e^2/m_j^*$ and $1/\tau_{D,j}$ are the square of the plasma frequency and scattering rate for the delocalized (Drude) carriers in the jth band, respectively; n_j and m_j^* are the carrier concentration and effective mass, respectively; and ω_k, γ_k, and Ω_k are the position, width, and strength of the kth vibration, respectively. The complex conductivity is $\tilde{\sigma}(\omega) = \sigma_1 + i\sigma_2 = -i\omega[\tilde{\epsilon}(\omega) - \epsilon_\infty]/60$ (in units of Ω^{-1} cm^{-1}).

The fits to the optical conductivity are complicated somewhat by the broad, overlapping nature of the bound excitations and the free-carrier components; indeed, the strong contribution from the bound excitations prevents us from analyzing the low-frequency conductivity in terms of the Hund's metal power-law frequency dependence discussed in Sec. I [18]. In an effort to deal with this issue, the optical conductivity has first
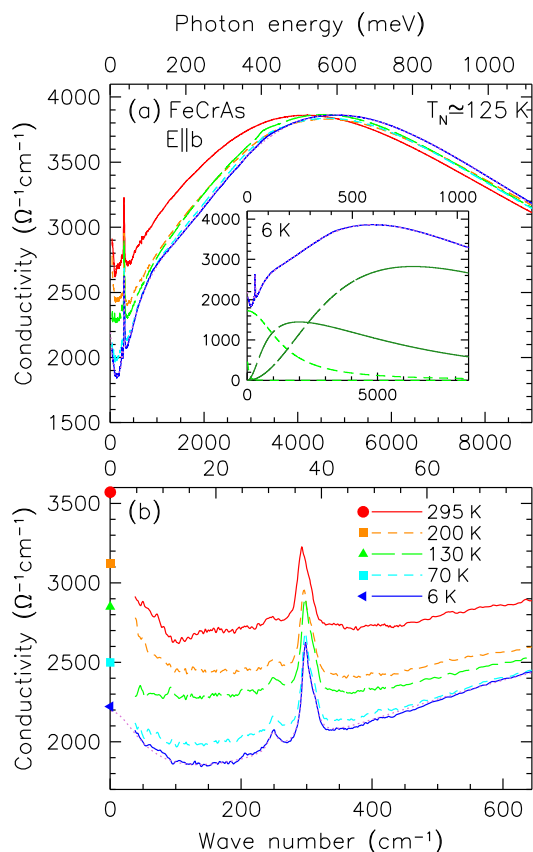
FIG. 6. (Color online) (a) The temperature dependence of the real part of the optical conductivity of FeCrAs for light polarized along the b axis over a wide frequency range; note the shoulder that becomes visible at $\simeq 0.12$ eV at or below T_N. The dotted line indicates the model fit to the optical conductivity at 6 K. Inset: the decomposition of the fit to the conductivity at 6 K into two Drude components (dashed lines) and two Lorentzian oscillators (dash-dotted lines). (b) The temperature dependence of the real part of the optical conductivity shown below 80 meV; the dotted line is the result of the fit to the data at 6 K. The symbols at the origin indicate the transport values for σ_{dc} along this crystalline axis.

been fit using a nonlinear least-squares technique at 6 K, where, in addition to the features observed at room temperature, a strong shoulder is observed in the optical conductivity at $\simeq 0.12$ eV. The most reliable fit is achieved by using two Drude components and two Lorentz oscillators; the fit over a wide frequency range is shown by the dotted line in Fig. 6(a). The Drude components consist of a strong broad component with $\omega_{p,D;1} \simeq 11\,740$ cm^{-1} and $1/\tau_{D,1} \simeq 1370$ cm^{-1}, and a much weaker narrow component with $\omega_{p,D;2} \simeq 1460$ cm^{-1} and $1/\tau_{D,2} \simeq 65$ cm^{-1}, while the parameters for the two Lorentz oscillators are $\omega_{L,1} \simeq 1950$ cm^{-1}, $\gamma_{L,1} \simeq 6670$ cm^{-1}, and $\Omega_{L,1} \simeq 24\,130$ cm^{-1} and $\omega_{L,2} \simeq 6360$ cm^{-1}, $\gamma_{L,2} \simeq 15\,380$ cm^{-1}, and $\Omega_{L,2} \simeq 50\,980$ cm^{-1} (Table II). The individual contributions to the optical conductivity are shown in the inset of Fig. 6(a). It is immediately apparent that the overdamped Lorentz oscillators show a considerable amount of overlap with the broad Drude component. We note that while the strong Drude component can reproduce most of the low-frequency conductivity, the Drude value for $\sigma_1(\omega \to 0) \equiv$

TABLE II. The temperature dependence along the b and c axes of the Drude scattering rates $1/\tau_{D,j}$, as well as the frequencies and damping strong mid-infrared electronic absorptions $\omega_{L,k}$ and $\gamma_{L,k}$. All units are in cm^{-1} unless otherwise indicated.[a]

T (K)	$1/\tau_{D,1}$	$1/\tau_{D,2}$	$\omega_{L,1}$	$\gamma_{L,1}$	$\omega_{L,2}$	$\gamma_{L,2}$
			$E \parallel b$			
295	900	~35	1850	4850	6590	15630
200	1000	~45	2050	5340	6760	15560
130	1080	~55	2080	5740	6530	15610
70	1270	~60	2040	6480	6350	15680
6	1370	~65	1950	6670	6360	15380
			$E \parallel c$			
T (K)	$1/\tau_{D,1}$	$1/\tau_{D,2}$	$\omega_{L,1}$	$\gamma_{L,1}$	$\omega_{L,2}$	$\gamma_{L,2}$
295	350	~60	1340	4420	6590	15120
200	400	~80	1490	4540	6640	15030
130	440	~90	1580	4650	6700	15070
70	410	~70	1530	4710	6830	15330
6	400	~80	1510	4690	6760	15110

[a]For $E \parallel b$: $\omega_{p,D;1} \simeq 11\,740$ cm^{-1}, $\omega_{p,D;2} \approx 1460$ cm^{-1}, $\Omega_{L,1} \simeq 24\,130$ cm^{-1}, and $\Omega_{L,2} \simeq 50\,980$ cm^{-1} are constant. For $E \parallel c$: $\omega_{p,D;1} \simeq 7090$ cm^{-1}, $\omega_{p,D;2} \simeq 1450$ cm^{-1}, $\Omega_{L,1} \simeq 26\,640$ cm^{-1}, and $\Omega_{L,2} \simeq 48\,610$ cm^{-1} are also fixed.

$\omega_{p,D}^2 \tau_D / 60 \simeq 1680$ Ω^{-1} cm^{-1} is well below the measured transport value of $\sigma_{dc} \simeq 2200$ Ω^{-1} cm^{-1}. The second, weak Drude component accurately reproduces the slight upturn in the optical conductivity observed at low frequency, and $1/\tau_{D,2}$ has been further fit to ensure that $\sigma_1(\omega \to 0) \simeq \sigma_{dc}$. This extrapolation is shown by the dotted line in Fig. 6(b), where the low-frequency conductivity is described quite well. Comparing the two Lorentz oscillators, we note that the majority of the spectral weight is associated with the high-frequency oscillator, $(\Omega_{L,1}/\Omega_{L,2})^2 \simeq 4.5$. In order to perform similar fits for the remaining temperatures, a constraint has been introduced on the fitting process by assuming that the Drude plasma frequencies and the strengths of the Lorentzian oscillators do not change; only the Drude scattering rates and the frequencies and widths of the Lorentz oscillators have been allowed to vary. The results of the fits using this convention are tabulated in Table II.

In addition to the strong electronic absorptions, there are several sharp features shown in more detail in Fig. 6(b) that are resolved as three separate vibrations. At 295 K, they are centered at $\simeq 246$, 292, and 302 cm^{-1}. The fitted parameters for these modes are listed in Table III at 295, 130, and 6 K. FeCrAs crystallizes in the hexagonal $P\bar{6}2m$ space group [31–33], so the irreducible vibrational representation is

$$\Gamma_{\text{vib}} = 2A_1' + 2A_2' + 6E' + A_1'' + 3A_2'' + 2E''.$$

Of these, only the E' and A_2'' vibrations are infrared active along the a-b planes and c axis, respectively. Thus, the three modes we observe in this polarization along the b axis are the normally infrared-active E' modes. The 292 and 302 cm^{-1} modes shift to slightly higher frequencies with decreasing temperature, but do not display any anomalous behavior at T_N. The 246 cm^{-1} mode also increases in frequency as the temperature is reduced; however, below T_N, this mode begins to decrease in frequency

TABLE III. The vibrational parameters for the fits to infrared-active modes in the optical conductivity of FeCrAs along the b and c axis between 295 and 6 K, where ω_k, γ_k, and Ω_k are the frequency, width, and strength of the kth mode, respectively. All units are in cm^{-1}.

				$E \parallel b$, E'				
	295 K			130 K			6 K	
ω_k	γ_k	Ω_k	ω_k	γ_k	Ω_k	ω_k	γ_k	Ω_k
245.8	27.8	346	250.9	23.2	345	248.5	16.7	342
291.6	14.9	604	296.9	12.0	604	297.9	11.2	603
302.0	18.2	498	307.4	16.7	498	309.1	18.0	496
				$E \parallel c$, A_2''				
	295 K			130 K			6 K	
ω_k	γ_k	Ω_k	ω_k	γ_k	Ω_k	ω_k	γ_k	Ω_k
123.5	7.9	540	125.9	7.2	580	127.0	5.4	580
263.5	22.5	530	267.2	17.9	510	270.5	19.3	510
318.0	25.4	960	321.4	19.6	980	322.4	17.0	990

FIG. 7. (Color online) The log-log plot of the temperature dependence of the real part of the optical conductivity vs wave number ($\bar{\nu} = 1/\lambda$) in the mid- and near-infrared regions for FeCrAs for light polarized along the b axis. Above about 0.7 eV, the power-law behavior $\sigma_1(\omega) \propto \omega^{-0.6}$ is clearly displayed. Inset: The same plot for $E \parallel c$.

with decreasing temperature. Strong spin-phonon interactions are expected to manifest themselves as either anomalous frequency shifts with the onset of magnetic order, or the appearance of Fano-like asymmetric line shapes [43–48]. The temperature dependence of the 246 cm^{-1} mode suggests weak spin-phonon coupling.

Returning to the optical conductivity, at room temperature, two broad Lorentz oscillators are observed at $\omega_{L,1} \simeq 1850$ cm^{-1} and $\omega_{L,2} \simeq 6590$ cm^{-1}, with broad ($1/\tau_{D,1} \simeq 900$ cm^{-1}) and narrow ($1/\tau_{D,2} \simeq 35$ cm^{-1}) Drude components. The majority of the free-carrier spectral weight is associated with the broad Drude component, where the spectral weight is defined as the area under the conductivity curve over a given interval, $N(\omega) = \int_0^\omega \sigma_1(\omega') d\omega'$. The ratio of the two different spectral weights will be proportional to $(\omega_{p,D;1}/\omega_{p,D;2})^2 \simeq 65$. As the temperature is lowered to just above T_N, the scattering rate for the strong Drude term has increased to $1/\tau_{D,1} \simeq 1080$ cm^{-1}, while the scattering rate for the weaker Drude term is also somewhat larger. These changes are reflected in the drop in the low-frequency conductivity and the decrease in σ_{dc}, as well as the transfer of spectral weight from low to high frequency. In comparison, the first Lorentz oscillator has increased in frequency to $\omega_{L,1} \simeq 2080$ cm^{-1}, but more interesting is the increase in the width to $\gamma_{L,1} \simeq 5740$ cm^{-1}. The high-frequency oscillator changes relatively little.

As the temperature is reduced below T_N, the resistivity along this direction continues to increase. This is reflected in the increase in the scattering rates for both Drude terms (Table II) and the continued decrease in the low-frequency conductivity. At or below T_N, a shoulder becomes clearly visible at about 0.12 eV in Fig. 6(a). In this analysis, we have assumed that this absorption is present at all temperatures; however, it could be the case that this feature is associated with the partial gapping of the Fermi surface below T_N due to the magnetic (and possible charge) order. We find no evidence for this scenario because there is no effective transfer of spectral weight from below this feature to energies above it, as would be expected for a transport gap (full or partial). This transfer of
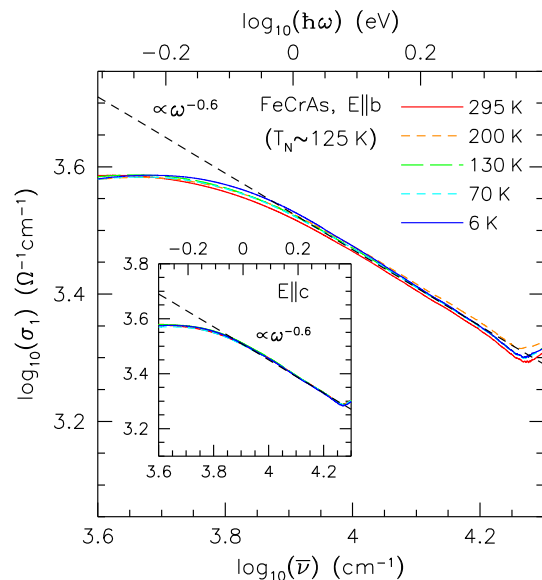
spectral weight is observed in BaFe$_2$As$_2$ below $T_{SDW} \simeq 138$ K due to the partial gapping of the Fermi surface [25,26]. We therefore conclude that the carrier concentration in the bands is not changing and the constraint on $\omega_{p,D;j}$ is valid. It is likely that this feature is a low-lying interband transition similar to those observed in Ba(Fe$_{1-x}$Co$_x$)$_2$As$_2$ [49]. The change in position and width of the low-frequency Lorentzian oscillator is probably due to the effects of Pauli blocking with increasing temperature (this is in accord with the observation that the high-frequency oscillator displays relatively little temperature dependence). The appearance of this feature below T_N is thus a consequence of the depletion of low-frequency spectral weight due to the broadening of the strong Drude component. The nonmetallic resistivity is due to Drude scattering rates that increase with decreasing temperature.

In the earlier discussion of the Hund's metal, it was remarked that at high frequencies in the incoherent regime, the optical conductivity is expected to exhibit an unusual power-law behavior, $\sigma_1(\omega) \propto \omega^{-\alpha}$, with $0 < \alpha < 1$. Interestingly, the log-log plot of the real part of the optical conductivity shown in Fig. 7 displays just such a relationship between 6000–20 000 cm^{-1}, with $\sigma_1(\omega) \propto \omega^{-0.6}$. This exponent is similar to what has been observed in this region for a number of other pnictide and iron-chalcogenide materials [18]. In addition, we also note that spectral weight is transferred from low to high frequency (i.e., above 6000 cm^{-1}) as the temperature is lowered to just above T_N [Fig. 6(a)]. This effect has also been observed in electron- and hole-doped BaFe$_2$As$_2$, where it is argued that this energy scale is simply the Hund's coupling J [50,51]. However, as previously discussed, the transfer of spectral weight is likely the result of the increase of the free-carrier scattering rate(s) with decreasing temperature. It may also be the case that this frequency region
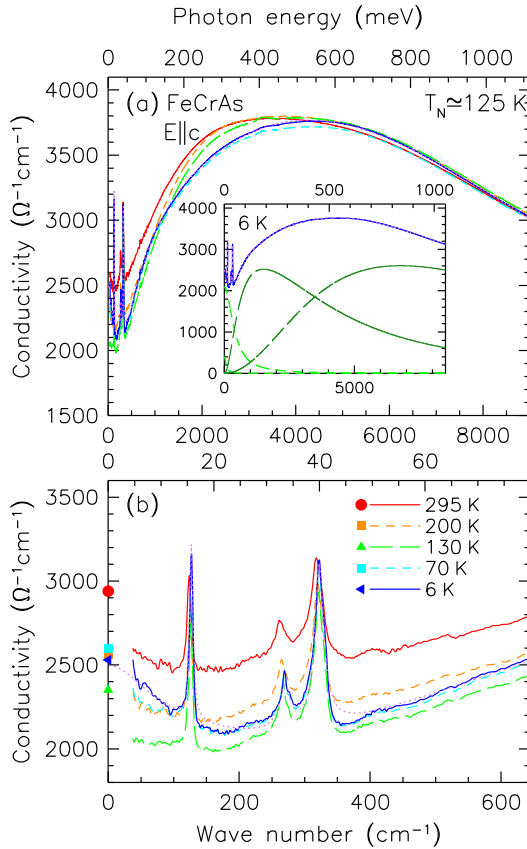
FIG. 8. (Color online) (a) The temperature dependence of the real part of the optical conductivity of FeCrAs for light polarized along the c axis over a wide frequency range. The dotted line indicates the model fit to the optical conductivity at 6 K. Inset: The decomposition of the conductivity at 6 K into two Drude components (dashed lines) and two Lorentzian oscillators (dash-dotted lines). (b) The temperature dependence of the real part of the optical conductivity shown below 80 meV; the dotted line is the fit to the 6 K data. The symbols at the origin indicate the transport values for σ_{dc} along the c axis.

is dominated by interband transitions described by the two Lorentzian oscillators used to fit the conductivity, and that it is the overlapping tails of these features that produce this fractional power law.

B. $E \parallel c$

The temperature dependence of the real part of the optical conductivity for light polarized along the c axis is shown in Fig. 8(a). The low-frequency conductivity is shown in Fig. 8(b), where the symbols at the origin denote the values for σ_{dc} determined from transport measurements (Fig. 1). A comparison with Fig. 6 indicates that both the electronic and vibrational properties of FeCrAs are anisotropic. The same methodology that was used to fit the optical conductivity for the b-axis polarization is used for this polarization as well. The optical conductivity at 6 K is once again described by two Drude terms and two Lorentz oscillators. The Drude components consist of a broad, strong term with $\omega_{p,D;1} \simeq 7090$ cm^{-1} and $1/\tau_{D,1} \simeq 400$ cm^{-1}, with a weaker component with $\omega_{p,D;2} \simeq 1450$ cm^{-1} and $1/\tau_{D,2} \simeq 80$ cm^{-1}. However, the ratio of the

strengths is now much smaller, $(\omega_{p,D;1}/\omega_{p,D;2})^2 \simeq 24$. The parameters for the two overdamped Lorentz oscillators at 6 K are $\omega_{L,1} \simeq 1510$ cm^{-1}, $\gamma_{L,1} \simeq 4690$ cm^{-1}, and $\Omega_{L,1} \simeq 26\,640$ cm^{-1} and $\omega_{L,2} \simeq 6760$ cm^{-1}, $\gamma_{L,2} \simeq 15\,110$ cm^{-1}, and $\Omega_{L,2} \simeq 48\,610$ cm^{-1} (Table II). We also note that the strengths of the two oscillators are more evenly matched, with $(\Omega_{L,2}/\Omega_{L,1})^2 \simeq 3.3$.

The individual contributions to the optical conductivity at 6 K are shown in the inset of Fig. 6(a). As outlined before, the fits to the optical conductivity at the remaining temperatures have been performed by allowing only the Drude widths and the frequencies and positions of the Lorentz oscillators to vary; the strengths are fixed. The results are summarized in Table II.

From room temperature to just above T_N, the scattering rate for the strong Drude term increases only slightly from $1/\tau_{D,1} \simeq 350$ to 440 cm^{-1}, while the weaker Drude term similarly increases from $1/\tau_{D,2} \simeq 60$ to 90 cm^{-1}. At the same time, the low-frequency oscillator shifts from $\omega_{L,1} \simeq 1340$ to 1580 cm^{-1}, while the damping remains more or less the same. The high-frequency oscillator shows little temperature dependence. As the temperature is lowered below T_N, the resistivity along this lattice direction decreases before slowly increasing again at low temperature. This is reflected in the decrease in the scattering rate of the strong Drude component $1/\tau_{D,1} \simeq 400$ cm^{-1} at 6 K, while the scattering rate for the weak Drude term first decreases to $1/\tau_{D,2} \simeq 70$ cm^{-1}, before increasing slightly to $\simeq 80$ cm^{-1} at 6 K. Below T_N, the oscillators display little temperature dependence. At or below T_N, a weak shoulder is observed in the optical conductivity at about 0.12 eV. Once again, there is no appreciable transfer of spectral weight from low to high frequency associated with this feature, ruling out the possibility of a transport gap, and it is argued that this structure becomes visible as a consequence of the broadening of the Drude terms at low temperature.

The optical conductivity in the high-frequency region again yields the unusual $\sigma_1(\omega) \propto \omega^{-0.6}$ power-law behavior (inset of Fig. 7). However, as was previously discussed, while this result is expected for a Hund's metal in the incoherent regime, it may also be the result of overlapping interband transitions.

The three sharp lattice modes shown in Fig. 8(b) are attributed to the normally infrared-active A_2'' modes. While the two modes at $\simeq 264$ and 318 cm^{-1} are similar in frequency to the E' modes observed in the b polarization, the mode at $\simeq 124$ cm^{-1} is much lower in energy and also considerably narrower (Table III). The modes increase in frequency with decreasing temperature and show no evidence of any anomalous behavior at T_N.

V. CONCLUSIONS

The optical properties of FeCrAs reveal a weakly anisotropic material at room temperature. Electronic structure calculations for FeCrAs show that this system is a metal with two bands crossing ϵ_F and a nonzero density of states; however, the temperature dependence of the resistivity exhibits a nonmetallic response. The multiband nature of this material allows the optical properties to be fit using a two-Drude model which yields a strong, broad term that extends well into the mid-infrared region, and a much weaker, narrower term that is necessary to describe the upturn in the

low-frequency conductivity as well as to yield the correct values for the dc conductivity. The mid-infrared region may be modeled using two bound excitations. At room temperature, the strong excitation is at about $\simeq 0.8$ eV in the planes and is almost identical along the c axis; this feature displays little temperature dependence. At or below T_N, a shoulder becomes visible in $\sigma_1(\omega)$ at $\simeq 0.12$ eV in both polarizations. However, the absence of any transfer of spectral weight from below to above this energy below T_N suggests that it is not associated with the opening of a partial gap and its emergence is instead attributed to the broadening of the Drude components with decreasing temperature. Superimposed on the optical conductivity are a number of sharp absorptions due to the normally infrared-active E' and A_2'' modes in the a-b planes and

along the c axis, respectively. In contrast to the modes that are observed to increase in frequency with decreasing temperature and show no anomalous behavior at T_N, the low-frequency E' mode at $\simeq 246\ \mathrm{cm}^{-1}$ softens below T_N, which is suggestive of spin-phonon coupling.

[1] Y. Ando, G. S. Boebinger, A. Passner, T. Kimura, and K. Kishio, Phys. Rev. Lett. **75**, 4662 (1995).

[2] V. Dobrosavljevic, in *Conductor Insulator Quantum Phase Transitions*, edited by V. Dobrosavljevic and N. Trivedi (Oxford University Press, Oxford, U.K., 2012).

[3] M. B. Maple, M. C. Deandrade, J. Herrmann, Y. Dalichaouch, D. A. Gajewski, C. L. Seaman, R. Chau, R. Movshovich, M. C. Aronson, and R. Osborn, J. Low. Temp. Phys. **99**, 223 (1995).

[4] N. F. Mott, Phil. Mag. **22**, 7 (1970).

[5] R. Rosenbaum, S. Mi, B. Grushko, and B. Przepiózynński, J. Low. Temp. Phys. **149**, 314 (2007).

[6] G. R. Stewart, Rev. Mod. Phys. **83**, 1589 (2011).

[7] W. Wu, A. McCollam, I. Swainson, P. M. C. Rourke, D. G. Rancourt, and S. R. Julian, Europhys. Lett. **85**, 17009 (2009).

[8] P. Nozières, J. Low. Temp. Phys. **17**, 31 (1974).

[9] I. P. Swainson, W. Wu, A. McCollam, and S. R. Julian, Can. J. Phys. **88**, 701 (2010).

[10] F. F. Tafti, W. Wu, and S. R. Julian, J. Phys.: Condens. Matter **25**, 385601 (2013).

[11] J. G. Rau and H.-Y. Kee, Phys. Rev. B **84**, 104448 (2011).

[12] A. H. Nevidomskyy and P. Coleman, Phys. Rev. Lett. **103**, 147205 (2009).

[13] L. Craco and S. Leoni, Europhys. Lett. **92**, 67003 (2010).

[14] Z. P. Yin, K. Haule, and G. Kotliar, Nat. Mater. **10**, 932 (2011).

[15] K. Haule, J. H. Shim, and G. Kotliar, Phys. Rev. Lett. **100**, 226402 (2008).

[16] K. Haule and G. Kotliar, New J. Phys. **11**, 025021 (2009).

[17] I. Okada and K. Yosida, Prog. Theor. Phys. **49**, 1483 (1973).

[18] Z. P. Yin, K. Haule, and G. Kotliar, Phys. Rev. B **86**, 195141 (2012).

[19] M. Dressel and G. Grüner, *Electrodynamics of Solids* (Cambridge University Press, Cambridge, U.K., 2001).

[20] S. Graser, A. F. Kemper, T. A. Maier, H.-P. Cheng, P. J. Hirschfeld, and D. J. Scalapino, Phys. Rev. B **81**, 214503 (2010).

[21] D. C. Johnston, Adv. Phys. **59**, 803 (2010).

[22] M. Rotter, M. Tegel, D. Johrendt, I. Schellenberg, W. Hermes, and R. Pöttgen, Phys. Rev. B **78**, 020503(R) (2008).

[23] M. A. Tanatar, N. Ni, G. D. Samolyuk, S. L. Bud'ko, P. C. Canfield, and R. Prozorov, Phys. Rev. B **79**, 134528 (2009).

[24] P. Richard, K. Nakayama, T. Sato, M. Neupane, Y.-M. Xu, J. H. Bowen, G. F. Chen, J. L. Luo, N. L. Wang, X. Dai, Z. Fang, H. Ding, and T. Takahashi, Phys. Rev. Lett. **104**, 137001 (2010).

[25] W. Z. Hu, J. Dong, G. Li, Z. Li, P. Zheng, G. F. Chen, J. L. Luo, and N. L. Wang, Phys. Rev. Lett. **101**, 257005 (2008).

[26] A. Akrap, J. J. Tu, L. J. Li, G. H. Cao, Z. A. Xu, and C. C. Homes, Phys. Rev. B **80**, 180502 (2009).

[27] C. C. Homes, T. Timusk, X. Wu, Z. Altounian, A. Sahnoune, and J. O. Ström-Olsen, Phys. Rev. Lett. **67**, 2694 (1991).

[28] T. Timusk, J. P. Carbotte, C. C. Homes, D. N. Basov, and S. G. Sharapov, Phys. Rev. B **87**, 235121 (2013).

[29] W. Wu, A. McCollam, I. P. Swainson, and S. R. Julian, in *Solid Compounds of Transition Elements*, Solid State Phenomena Vol. 170, edited by J. L. Bobet, B. Chevalier, and D. Fruchart (Trans Tech Publications, Switzerland, 2011), pp. 276–281.

[30] C. C. Homes, M. Reedyk, D. A. Crandles, and T. Timusk, Appl. Opt. **32**, 2976 (1993).

[31] L. Hollan, Ann. Chim. (Paris) **1**, 437 (1966).

[32] M. Nylund, M. Roger, J. Sénateur, and R. Fruchart, J. Solid State Chem. **4**, 115 (1972).

[33] R. Guérin and M. Sergent, Mater. Res. Bull. **12**, 381 (1977).

[34] P. B. Littlewood and C. M. Varma, J. Appl. Phys. **69**, 4979 (1991).

[35] F. Wooten, *Optical Properties of Solids* (Academic, New York, 1972), pp. 244–250.

[36] D. J. Singh, *Planewaves, Pseudopotentials and the LAPW Method* (Kluwer Adademic, Boston, 1994).

[37] D. Singh, Phys. Rev. B **43**, 6388 (1991).

[38] P. Blaha, K. Schwarz, G. K. H. Madsen, D. Kvasnicka, and J. Luitz, WIEN2k, *An Augmented Plane Wave Plus Local Orbitals Program for Calculating Crystal Properties* (Technische Universität Wien, Austria, 2001).

[39] S. Ishida, T. Takiguchi, S. Fujii, and S. Asano, Physica B **217**, 87 (1996).

[40] J. W. Allen and J. C. Mikkelsen, Phys. Rev. B **15**, 2952 (1977).

[41] A. V. Puchkov, D. N. Basov, and T. Timusk, J. Phys.: Condens. Matter **8**, 10049 (1996).

[42] D. Wu, N. Barišić, P. Kallina, A. Faridian, B. Gorshunov, N. Drichko, L. J. Li, X. Lin, G. H. Cao, Z. A. Xu, N. L. Wang, and M. Dressel, Phys. Rev. B **81**, 100512 (2010).

[43] J. W. Bray, L. V. Iterrante, I. S. Jacobs, and J. C. Bonner, in *Extended Linear Chain Compounds*, edited by J. S. Miller (Plenum, New York, 1983), pp. 353–415.

[44] C. C. Homes, M. Ziaei, B. P. Clayman, J. C. Irwin, and J. P. Franck, Phys. Rev. B **51**, 3140 (1995).

[45] A. B. Kuz'menko, D. van der Marel, P. J. M. van Bentum, E. A. Tishchenko, C. Presura, and A. A. Bush, Phys. Rev. B **63**, 094303 (2001).

[46] K.-Y. Choi, Y. G. Pashkevich, K. V. Lamonova, H. Kageyama, Y. Ueda, and P. Lemmens, Phys. Rev. B **68**, 104418 (2003).

[47] A. B. Sushkov, O. Tchernyshyov, W. Ratcliff II, S. W. Cheong, and H. D. Drew, Phys. Rev. Lett. **94**, 137202 (2005).

[48] J. Kim, S. Jung, M. S. Park, S.-I. Lee, H. D. Drew, H. Cheong, K. H. Kim, and E. J. Choi, Phys. Rev. B **74**, 052406 (2006).

[49] P. Marsik, C. N. Wang, M. Rössle, M. Yazdi-Rizi, R. Schuster, K. W. Kim, A. Dubroka, D. Munzar, T. Wolf, X. H. Chen, and C. Bernhard, Phys. Rev. B **88**, 180508(R) (2013).

[50] N. L. Wang, W. Z. Hu, Z. G. Chen, R. H. Yuan, G. Li, G. F. Chen, and T. Xiang, J. Phys.: Condens. Matter **24**, 294202 (2012).

[51] A. A. Schafgans, S. J. Moon, B. C. Pursley, A. D. LaForge, M. M. Qazilbash, A. S. Sefat, D. Mandrus, K. Haule, G. Kotliar, and D. N. Basov, Phys. Rev. Lett. **108**, 147002 (2012).